Monthly Notices
of the
ROYAL ASTRONOMICAL SOCIETY

MNRAS **456,** 4533–4541 (2016) doi:10.1093/mnras/stv2931

KROSS: mapping the Hα emission across the star formation sequence at $z \approx 1$

Georgios E. Magdis,[1,2,3★] Martin Bureau,[1] J. P. Stott,[1,4] A. Tiley,[1] A. M. Swinbank,[4,5] R. Bower,[4,5] A. J. Bunker,[1†] Matt Jarvis,[1,6] Helen Johnson[5] and Ray Sharples[4,7]

[1]*Department of Physics, University of Oxford, Keble Road, Oxford OX1 3RH, UK*
[2]*Dark Cosmology Centre, Niels Bohr Institute, University of Copenhagen, Juliane Mariesvej 30, DK-2100 Copenhagen, Denmark*
[3]*Institute for Astronomy, Astrophysics, Space Applications and Remote Sensing, National Observatory of Athens, GR-15236 Athens, Greece*
[4]*Institute for Computational Cosmology, Durham University, South Road, Durham DH1 3LE, UK*
[5]*Centre for Extragalactic Astronomy, Department of Physics, Durham University, South Road, Durham DH1 3LE, UK*
[6]*Department of Physics, University of the Western Cape, Bellville 7535, South Africa*
[7]*Centre for Advanced Instrumentation, Department of Physics, Durham University, South Road, Durham DH1 3LE, UK*

Accepted 2015 December 12. Received 2015 December 12; in original form 2015 July 17

ABSTRACT

We present first results from the KMOS (*K*-band Multi-Object Spectrograph) Redshift One Spectroscopic Survey, an ongoing large kinematical survey of a thousand, $z \sim 1$ star-forming galaxies, with VLT KMOS. Out of the targeted galaxies (∼500 so far), we detect and spatially resolve Hα emission in ∼90 and 77 per cent of the sample, respectively. Based on the integrated Hα flux measurements and the spatially resolved maps, we derive a median star formation rate (SFR) of ∼7.0 $M_\odot$ yr^{-1} and a median physical size of $\langle r'_{1/2} \rangle = 5.1$ kpc. We combine the inferred SFRs and effective radii measurements to derive the star formation surface densities (Σ_{SFR}) and present a 'resolved' version of the star formation main sequence (MS) that appears to hold at subgalactic scales, with similar slope and scatter as the one inferred from galaxy-integrated properties. Our data also yield a trend between Σ_{SFR} and Δ(sSFR) (distance from the MS) suggesting that galaxies with higher sSFR are characterized by denser star formation activity. Similarly, we find evidence for an anticorrelation between the gas phase metallicity (*Z*) and the Δ(sSFR), suggesting a 0.2 dex variation in the metal content of galaxies within the MS and significantly lower metallicities for galaxies above it. The origin of the observed trends between Σ_{SFR}–Δ(sSFR) and *Z*–Δ(sSFR) could be driven by an interplay between variations of the gas fraction or the star formation efficiency of the galaxies along and off the MS. To address this, follow-up observations of our sample that will allow gas mass estimates are necessary.

Key words: Galaxy: evolution.

1 INTRODUCTION

A recent major step forward in understanding the nature of star formation in distant galaxies has been the discovery that the majority of star-forming galaxies show a strong correlation between their star formation rate (SFR) and their stellar mass (M_*) from $z = 0$ to 7 (e.g. Brinchmann et al. 2004; Daddi et al. 2007; Elbaz et al. 2007; Noeske et al. 2007; Pannella et al. 2009; Magdis et al. 2010; Whitaker et al. 2014). This correlation, the star formation sequence or the main sequence (MS) of star formation, is characterized by an increasing normalization factor (parametrized by the specific star formation rate, sSFR ≡ SFR/M_*) with lookback time (e.g. González et al. 2010; Elbaz et al. 2011) and a rather small and constant scatter of 0.3 dex at all redshifts and stellar masses (e.g. Schreiber et al. 2015). The tightness of this correlation, that speaks against stochastic merger-induced star-forming episodes as the main driver of star formation activity, has been put forward as indirect evidence for secular galaxy evolution (e.g. Noeske et al. 2007).

The contrasting nature of MS galaxies to that of galaxies that, due to their enhanced sSFRs, lie above the MS (hereafter starburst galaxies), is manifested in terms of various sets of observables.

★E-mail: georgios.magdis@astro.ox.ac.uk
† Affiliate Member, Kavli Institute for the Physics and Mathematics of the Universe, 5-1-5 Kashiwanoha, Kashiwa 277-8583, Japan.

As galaxies depart from the MS, they appear to have higher total-to-mid-infrared (IR) luminosity ratio, IR8 $\equiv L_{\rm IR}/L_8$ (Elbaz et al. 2011; Nordon et al. 2012, where $L_{\rm IR}$ and L_8 are the total IR and the rest-frame 8 μm luminosity, respectively), weaker far-IR atomic lines (e.g. Gracia-Carpio et al. 2011; De Looze et al. 2014; Magdis et al. 2014), higher star formation efficiencies (SFEs $\equiv$ SFR/$M_{\rm H_2}$; Daddi et al. 2010; Genzel et al. 2010; Magdis et al. 2012 b) and higher dust temperatures (e.g. Magdis et al. 2012b; Magnelli et al. 2014). Furthermore, morphological studies have shown a trend of increasing incidence of interacting/merging systems as a function of distance from the MS (Hung et al. 2013; Stott et al. 2013a). In that respect, there is a trend towards a new paradigm where the properties of the galaxies are not, as traditionally thought, just linked to their IR luminosities (or SFRs), but rather to their specific star formation rate (sSFR = SFR/M_*), or equally, to their position with respect to the MS.

The observed deviations of starbursts from the SFR–M_*, $L_{\rm IR}$–L_8, $L_{\rm IR}$–$L_{\rm CII}$ and $L_{\rm IR}$–$L'_{\rm CO}$ scaling laws, that are followed by the majority of star-forming galaxies at all redshifts and luminosities, have been interpreted as evidence of more intense star formation, more compact geometries and higher star formation surface densities, probably triggered by merger events (e.g. Noeske et al. 2007; Daddi et al. 2010; Genzel et al. 2010; Elbaz et al. 2011; Díaz-Santos et al. 2013; Magdis et al. 2014). In particular, Elbaz et al. (2011), using radio and mid-IR observations, found a clear correlation between the projected SFR surface density ($\Sigma_{\rm SFR}$) of local galaxies and their distance from the MS. Similarly, using stacking techniques, they showed that $z \approx 0.8$–1.5 starbursts are characterized by high, on average, IR surface brightness ($\Sigma_{\rm IR} > 3.0 \times 10^{10}$ L$_\odot$ kpc^{-2}), suggestive of compact star formation activity (Díaz-Santos et al. 2010).

However, how (and if) the $\Sigma_{\rm SFR}$, as well as other physical properties such as the metal abundance of distant galaxies, varies within and outside the MS is still unclear. Here, we attempt to address this question, taking advantage of spatially resolved Hα observations of a large sample of $z \approx 1.0$ star-forming galaxies, as part of the ongoing KMOS (*K*-band Multi-Object Spectrograph) Redshift One Spectroscopic Survey (KROSS). Throughout the paper we adopt the *WMAP*-7 cosmology ($\Omega_{\rm m} = 0.273$, $\Omega_\Lambda + \Omega_{\rm m} = 1.0$, $\Omega_{\rm k} = 0$ and $H_0 = 70.4$ km s^{-1} Mpc^{-1}; Larson et al. 2011) and a Chabrier (2003) initial mass function (IMF).

2 SAMPLE, OBSERVATIONS AND DATA REDUCTION

KROSS is an ongoing study of ∼1000 mass-selected star-forming galaxies. The majority of the galaxies in the sample are selected to be brighter than a magnitude limit of $K_{\rm AB} \approx 22.5$ [that roughly corresponds to a limiting stellar mass of $\log(M_*/{\rm M}_\odot) > 9.3 \pm 0.5$], excluding sources identified as active galactic nuclei (AGNs; either spectroscopically or from their X-ray emission). Other than that, no other colour, or size cut, criterion was applied to the sample. While the redshift range of the sample spans from $z \approx 0.7$ to ≈1.5, 96 per cent of the galaxies lie within $0.8 < z < 1.0$, with a median of 0.86. The KROSS galaxies are selected from spectroscopic surveys in some of the most well-studied fields in thy sky. In particular, targets were drawn from the UDS (Ultra Deep Survey; Lawrence et al. 2007), ECDFS (Extended Chandra Deep Field South; Lehmer et al. 2005), COSMOS (Cosmological Evolution Survey; Scoville et al. 2007) and SA22 (Steidel et al. 1998). The number of sources from each field, as well as a reference to the corresponding spectroscopic survey, are listed in Table 1. We note that the selected galaxies consist a representative sample of typical star-forming galaxies at $z \sim 1$, exhibiting a similar distribution in colour ($r - z$), stellar mass (M_*) and SFR to that of the parent sample (see Stott et al., in preparation).

The KROSS survey commenced in 2013 November, exploiting the recently commissioned KMOS (Sharples et al. 2013), a near-IR integral field spectrograph on the VLT. The main aim of the survey is to target, primarily, the redshifted Hα and [N II] emission lines of $z \approx 1$ star-forming galaxies. A detailed description of the sample selection, the survey design and the data reduction is presented in Stott et al. (in preparation) and Tiley et al. (2015),

In this work, we employ data from the first 21 fields observed by KMOS as part of the KROSS survey, from 2013 November to 2014 November. During this period KMOS observed a total of 487 galaxies, employing 24 integral field units (IFUs) per field, each with a square field of view of 2.8 arcsec × 2.8 arcsec. The light from each set of eight IFUs, that are mounted in configurable arms with a patrol field of 7.2 arcmin in diameter, is dispersed in three cryogenic grating spectrometers. Our observations were carried out using the YJ filter with a spectral coverage of 1.01–1.35 μm at a spectral resolution of $\lambda/\Delta\lambda = 3300$. We adopted an ABA (object–sky–object) observing sequence, with 600 s integration per

Table 1. A list of the extragalactic fields observed by KROSS and the parent spectroscopic redshift catalogues from which we source our KMOS targets.

Field:	UDS	ECDFS	COSMOS	SA22
Coordinates (J2000):	02:17:48 −05:05:45	03:32:28 −27:48:30	10:00:28 +02:12:21	22:17:00 00:20:00
Redshift surveys				
	UDS[a]	MUSYC[b]	zCOSMOS[c]	VVDS[d]
	VIPERS[e]	VVDS[d]	HiZELS[f]	VIPERS[e]
	HiZELS[f]	–	–	CF-HiZELS[g]
Nmaster	7168	318	1743	8283
Nobs	149	120	102	116

[a]Smail et al. (2008), Akiyama et al. (in preparation) and Simpson et al. (in preparation).
[b]Cardamone et al. (2010) and references therein.
[c]Lilly et al. (2007).
[d]Le Fèvre et al. (2005, 2013) and Garilli et al. (2008).
[e]Garilli et al. (2014) and Guzzo et al. (2014).
[f]Sobral et al. (2012, 2013).
[g]Sobral et al. (2013, 2015) and Stott et al. (2014).

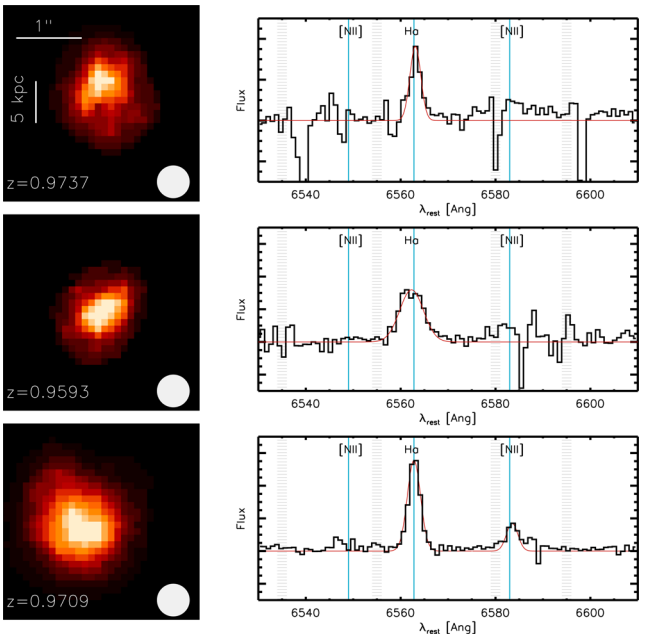

Figure 1. Hα emission map and the corresponding spectrum for three sources from our sample (below, on and above the MS). The spectra are truncated, showing only the wavelength range that covers the [N II] 6548.03 Å, Hα and [N II] 6583 Å lines, denoted with cyan vertical lines. The grey lines correspond to the locations of bright night sky lines, with a width that corresponds to the full width at half-maximum (FWHM) of the effective spectral resolution of the data. The thin red lines depict the best-fitting line profiles. The *x*-axis in the spectra has been shifted to the rest frame based on the measured redshift of each source. The grey circles on the maps, depict the PSF FWHM.

pointing. The total on-source integration time was typically 2.5-h per galaxy.

For data reduction we employed the ESOREX/SPARK (Davies et al. 2013). The software extracts the slices for each IFU and preforms flat-fielding, illumination correction and wavelength calibration of the data. Sky OH subtraction was optimized using a two-step approach. First we subtracted from each object IFU (A), its adjacent sky frame (B). Then, in order to improve the sky subtraction, for each pair of object minus sky (A−B) frames, we further subtracted the average residual between two sky positions. This technique was found to minimize the sky residuals from the final science products. For a detailed description of this method as well as alternative techniques to optimize the sky subtraction for KMOS data we refer the reader to Stott et al. (in preparation). The final (continuum subtracted) Hα map for each galaxy was subsequently created by centroiding wavelength-collapsed images around the redshifted Hα emission and combining each exposure (i.e. each data cube) using a clipped average. Both the effects of instrumental resolution and the spatial point spread function (PSF) were taken into account throughout the analysis and are included in the error estimation. Examples of spatially resolved Hα maps and the corresponding rest-frame integrated spectra, centred at redshifted Hα emission line, are shown in Fig. 1.

The data of the acquisition and telluric standard stars were reduced following the same procedure as for the science data. During each observation, typically one IFU was placed on a star to monitor the shape and variation of the PSF during the exposure. For each target, the spatial PSF was measured on the two-dimensional images of the acquisition and science stars, obtained by averaging

Table 2. Statistics of the properties for various subsamples of the observed KROSS galaxies.

	N	$< (r-z) >$	$< K >$	$< \mathrm{SFR_{SED}} >$
Total	487	0.98	21.1	4.8
Hα	437	0.95	21.2	6.8
Hα resolved	374	0.90	21.2	7.2
Hα unresolved	63	1.27	20.6	2.0
Hα undetected	50	1.32	20.5	1.2
[N II] (6583 Å)	190	0.95	21.3	6.0

(with σ-clipping) all the wavelength channels of the stars' reduced data cubes, by fitting Gaussian profiles. The effective angular resolution of our data sets from the PSF half-width at half-maximum (HWHM) ranges from 0.23 to 0.42 arcsec, with a mean of 0.31 arcsec (corresponding to ∼2–3.4 kpc and ∼2.5 kpc, respectively, at $z \approx 1$).

We fit the Hα 6563 Å and [N II] 6583 Å emission lines allowing the centroid, intensity and width of a Gaussian profile to vary as a free parameter (while keeping the central wavelength and the full width at half-maximum – FWHM – of the Hα and [N II] 6583 Å lines coupled in the fit). With this method we derived central wavelengths and integrated fluxes, while the corresponding uncertainties were estimated by perturbing the data points within their error bars, and repeating the fit. Overall we detected integrated Hα 6563 Å emission (signal to noise, S/N > 3) in 437 galaxies, of which 374 are also spatially resolved, while [N II] 6583 Å emission was detected in 190 galaxies. These numbers yield an Hα detection and resolving efficiency of ≈90 and ≈77 per cent, respectively, for the KROSS survey. In ∼4 per cent of the sample we only detect continuum emission while ∼6 per cent remain undetected. The median $r-z$ colour of the galaxies with resolved Hα emission is 0.90 while for those where Hα emission remains unresolved is 1.27. Furthermore, the median *K*-band magnitude for these two subsamples is 21.2 and 20.6, respectively. Finally, galaxies with no Hα detection or galaxies where Hα emission is unresolved have significantly lower SFRs (as derived from spectra energy distribution – SED – fitting; see Section 3.1) with a median value of ∼1.5 $\mathrm{M_\odot\ yr^{-1}}$, which is four to five times lower in comparison to the median SFR of galaxies with Hα detection (∼7.0 $\mathrm{M_\odot\ yr^{-1}}$). The redder $r-z$ colour, the brighter *K*-band magnitude and the significantly lower SFRs of the Hα unresolved/undetected population demonstrates that its the more massive and more passive galaxies that are characterized by weak Hα emission (see Table 2).

3 ANALYSIS

3.1 Stellar masses, attenuation and SFRs

Our targets benefit from extensive rest-frame UV to mid-IR photometric coverage. We built a multiwavelength catalogue (u, B, V, R, I, z, J, K + IRAC) using a 2.0 and 3.8-arcsec diameter aperture matched photometry in the optical/near-IR and IRAC bands, respectively (Cirasuolo et al. 2007; Cardamone et al. 2010; Kim et al. 2011b; Muzzin et al. 2013b; Simpson et al. 2014). The photometric bands were consistent between the fields except for SA22 where g was used instead of B and V and no suitable IRAC imaging was available.

The optical-to-near-IR data were then used to perform SED fitting to estimate each galaxy's stellar mass (M_*), dust extinction (A_V) and age. For this task, we employed the CIGALE code, which

fits photometric data points with synthetic stellar population models, and picks the best-fitting parameters by minimizing the χ^2 between observed and model fluxes. The models were built based on the Bruzual & Charlot (2003) library assuming a solar metallicity, a constant star formation history (SFH), a Calzetti et al. (2000) attenuation law and a minimum age of 0.3 Gyr. The stellar mass is obtained by integrating the modelled SFR over the galaxy age, and correcting for the mass-loss in the course of stellar evolution. As the derived parameters, especially SFR, are known to be sensitive to the choice of the SFH (e.g. Mancini et al. 2011), we repeated the analysis assuming a double exponentially rising SFH. While the absolute values of the derived parameters do vary between the two SFHs, the overall trends reported in this work remain unaffected. In the rest of the paper we use the stellar masses and A_V values derived assuming a constant SFH.

Repeating the fit including this time the AGN module of CIGALE in order to quantify the fraction of emission arising from possible AGN activity, does not change the derived properties. This was somewhat expected as from the parent sample we specifically excluded sources identified as AGNs, either spectroscopically or from their X-ray emission. Also, based on the [N II]/Hα flux ratio AGN diagnostics of Kewley et al. (2001), we find that none of the KROSS galaxies are identified as AGN as all have $\log([\mathrm{N\,II}]/\mathrm{H}\alpha) < 0.2$ (of which only nine have $0.0 < \log([\mathrm{N\,II}]/\mathrm{H}\alpha) < 0.2$).

Rather than using the indicative SFR derived through SED fitting, we measured the instantaneous SFR directly from the data using the Hα line measurements. The first step was to infer the observed Hα luminosity, $L_{\mathrm{H}\alpha,\mathrm{obs}}$, of each galaxy using the Hα flux extracted from the spatially integrated spectra. Since most of Hα emission is likely to originate from the H II regions that suffer from dust extinction, we derived intrinsic Hα luminosity, $L_{\mathrm{H}\alpha,\mathrm{int}}$, taking into account the stellar reddening A_V. In particular, following Wuyts et al. (2013), we converted the inferred stellar extinction to gas extinction (A_{gas}) and derived the corresponding L(Hα, int) through

$$A_{\mathrm{gas}} = A_V \times (1.9 - 0.15A_V), \quad (1)$$

$$L_{\mathrm{H}\alpha,\mathrm{obs}} = L_{\mathrm{H}\alpha,\mathrm{int}} \times 10^{-0.4A_{\mathrm{gas}}}. \quad (2)$$

Subsequently, we converted the intrinsic Hα luminosities to SFRs using the Kennicutt (1998) relation, scaled to a Chabrier IMF (Chabrier 2003):

$$\log(\mathrm{SFR})[\mathrm{M}_\odot \mathrm{yr}^{-1}] = \log(L_{\mathrm{H}\alpha,\mathrm{int}})[\mathrm{erg\ s}^{-1}] - 41.33. \quad (3)$$

The derived SFRs range from 0.15 to 330 $\mathrm{M}_\odot$ yr^{-1} with a median of $\sim$7.0 $\mathrm{M}_\odot$ yr^{-1}. A comparison between the Hα-based SFRs and those obtained through the SED fitting is shown in Fig. 2 (left), revealing an overall agreement between the two independent estimates.

In Fig. 2 (right), we also place our sources in the SFR–M_* plane along with the MS at the median redshift of our sample ($z = 0.86$) as prescribed by Speagle et al. (2014), taking into account the dependence of the MS on both the redshift and stellar mass of the galaxies. Evidently, the majority of our sources exhibit sSFR consistent with that of MS galaxies (within a factor of ≈ 2), with a few outliers both below and above the MS. This further demonstrates that the KROSS sample is representative of the population of typical star-forming galaxies at $z \sim 1$.

Finally, we tested a possible bias in our analysis introduced by the more modest sampling of the SED in SA22. First, we repeated whole analysis presented in this work but excluding this time the subsample of galaxies in SA22. Then we repeated the analysis only for galaxies that lie in SA22. In both cases, the trends and general

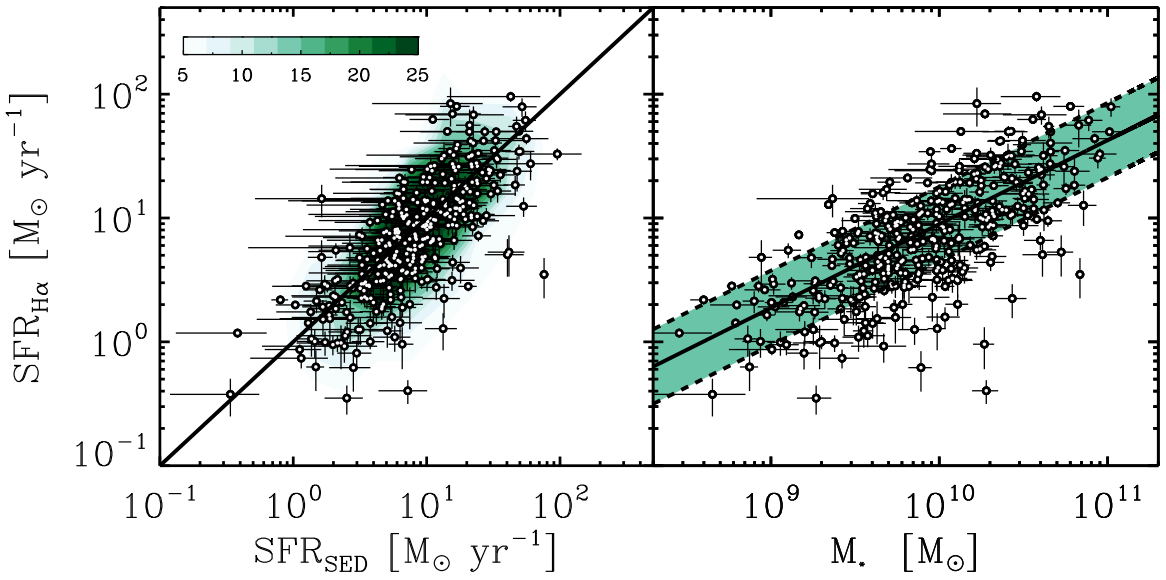

Figure 2. Left: comparison of SFRs as derived based on SED fitting and based on Hα flux measurements corrected for dust attenuation. The green contours depict the number density of the sources while the solid black line corresponds to the 1–1 correlation. Right: SFRs (based on dust corrected Hα measurements) versus the stellar masses of the galaxies in our sample. The solid line represents the star formation sequence at the median redshift of the sample ($z = 0.86$) along with a 0.3 scatter (dashed lines) as derived by Speagle et al. (2014), taking into account both the dependence on redshift and stellar mass. Evidently, our sources follow closely the SFR–M_* MS at this redshift.

conclusions remain unaffected with respect to those derived when using the whole sample.

3.2 Size estimates

To estimate the intrinsic Hα sizes of the sources ($r'_{1/2}$), we first determined the half-light radius of the Hα maps ($r_{1/2}$(Hα)) using the curve-of-growth analysis in elliptical apertures centred at the dynamical centre of the galaxies, as obtained by modelling the two-dimensional velocity field of each galaxy using a six parameter model (inclination, disc rotation speed, position angle, [*x*/*y*] centre and rotation curve shape; see Swinbank et al. 2012 for details). To derive the intrinsic sizes, $r'_{1/2}$, we then corrected the measured $r_{1/2}$(Hα) for the effective spatial resolution by subtracting in quadrature the PSF HWHM appropriate for each data set. As the shape of the PSF is known to vary among the three KMOS spectrographs we derived an average PSF for each spectrograph using the acquisition and the monitor stars at the appropriate IFUs.

For the measurement of intrinsic size of the galaxies we identify three sources of uncertainty. The first is the uncertainty associated with the size measurement of the galaxies through the growth of curve fitting. The second is the PSF variation during the observations of a particular field. Inspection of the PSFs associated with individual OBs of a given object suggests typical seeing variations of <20 per cent. Finally, the third source of uncertainty arises from the fact that in our analysis we assume that the PSF is axisymmetric, which is not always the case. Indeed, fitting a two-dimensional elliptical Gaussian to the PSFs we find that the ellipticity of the PSFs varied between 0.05 and 0.1 for spectrographs one and two and between 0.1 and 0.2 for spectrograph three. To derive the uncertainties of the intrinsic (physical) sizes we combine in quadrature the aforementioned errors, that are associated with the growth of curve analysis and the shape of the PSF. The average intrinsic size on our sample is 5.4 kpc (ranging from 1.4 to 22.3 kpc) with a corresponding uncertainty of ≈ 30 per cent. An obvious caveat of our analysis is that due to the seeing limited nature of our observations, we cannot spatially resolve individual star-forming clumps in our galaxies. Therefore, we cannot disentangle between a smooth disc-like distribution of the star formation activity and individual clumpy [H II] regions that are separated by a distance comparable to the size of our PSF.

To account for Hα flux missed due to low S/N at the outskirts of each galaxy we also modelled the curve of growth of each galaxy with a Gaussian radial distribution. In almost all cases >90 per cent of the extrapolated, integrated Hα flux is recovered by our data. As a sanity check, we also repeated the size measurements using two independent methods: first by using as centre of the curve of growth the centroid of the line emission as determined from the line maps, and secondly employing GALFIT to model the radial distribution of the Hα flux. The size measurements of the three methods are consistent within the uncertainties, without any obvious systematics. For the rest of this work, we thus adopt the size measurements based on the curve of growth analysis using the dynamical centre of the galaxies.

The analysis described above was applied to the whole sample of galaxies with Hα detection (437). A galaxy was considered resolved if the derived $r_{1/2}$(Hα) was larger than the HWHM of the corresponding PSF. In total we have 374 galaxies with resolved Hα emission. For the rest 63 unresolved sources, we adopt a size upper limit equal to the HWHM of the PSF.

Finally, we complement our Hα size measurements with stellar size estimates by matching our sample with the morphological catalogue of Van der Wel et al. (2012). This catalogue, produced using GALFIT (Peng et al. 2002), offers, among other parameters, half-light radius and Sérsic index measurements based on high resolution (0.17 arcsec) *HST*-WFC3 H_{F160W} filter observations, that trace the stellar continuum of the galaxies at $z \sim 0.8$–1.0 and therefore can serve as stellar size estimates. Out of the whole sample, we have both stellar and Hα size measurements for a subsample of 117 galaxies in the COSMOS, GOODS-S and UDS fields. For completeness, and to investigate possible biases introduced by the derivation of the stellar sizes based on the H_{F160W}-band observations, we also consider the GALFIT morphological analysis of Häußler et al. (2007) in ECDFS and Tasca et al. (2009) in COSMOS, based on (0.1 arcsec) *HST*-ACS *F*814*W* imaging. These studies offer structural information for 182 galaxies in our sample.

3.3 Metallicity

Using the [N II] to Hα emission line ratio we are also in position to estimate the gas phase abundance of oxygen [12+log(O/H)] (e.g. Kewley & Dopita 2002) in ∼190 galaxies from our sample for the which we have both [N II] and Hα detections. Using the Pettini & Pagel (2004) formula, 12+log[O/H] = 8.9+0.57 × *N*2, where *N*2= log($f_{[\mathrm{N\,II}]}/f_{\mathrm{H}\alpha}$), we derive individual metallicity estimates for each galaxy as well as an average metallicity for the sample of 8.64 ± 0.02, that is very close to solar metalliciy.

The lower detection rate of [N II] (≈40 per cent) compared to that of Hα (≈90 per cent), could imply a bias of the sample towards lower metallicity sources. However, the non-detection of [N II], could be affected by imperfect subtraction of strong OH sky lines (e.g. Stott et al. 2013b). Indeed, by measuring the distance of the [N II] central wavelength to that of strong (>20 relative strength) sky lines (Rousselot et al. 2000), we find an average distance of ≈7.5 Å for the galaxies that have no detection in [N II]. On the other hand, the average distance of the [N II] central wavelength for galaxies with [N II] detection is 11.7 Å. Given that the spectral resolution of KMOS in these wavelengths is ∼ 3.5 Å, it is likely that a large fraction of non-[N II] detections are affected from the presence of skylines. We find that among the 247 galaxies with no [N II] detection, for 113 the [N II] wavelength is less than 7 Å (2×FWHM) away from a strong skyline. These sources are subsequently omitted from the metallicity analysis. For the rest 134 galaxies with no [N II] but for which the [N II] wavelength is more than 7 Å (2×FWHM) away from a strong skyline, we derive a metallicity upper limit assuming a 5σ [N II] flux density, as derived from the noise of the spectrum at the corresponding wavelength.

4 RESULTS AND DISCUSSION

The main goal of this paper is to investigate if and how the width of the MS, as depicted in Fig. 2 (right), as well as the deviation from the MS, reflect variations in the physical properties of the galaxies. With key parameters at hand, such as SFR, stellar mass, physical size, metallicity and stellar mass, for a large sample of $z \sim 1$ star-forming galaxies, in this section we will first look into a resolved flavour of the MS and then proceed to explore possible variations of the star formation surface density and the metal abundance of the galaxies as we move along and above the MS of star formation.

4.1 A resolved MS of star formation

By combining the Hα-based SFRs with the Hα sizes, we can derive the star formation surface density (Σ_{SFR}), i.e. the amount of SFR

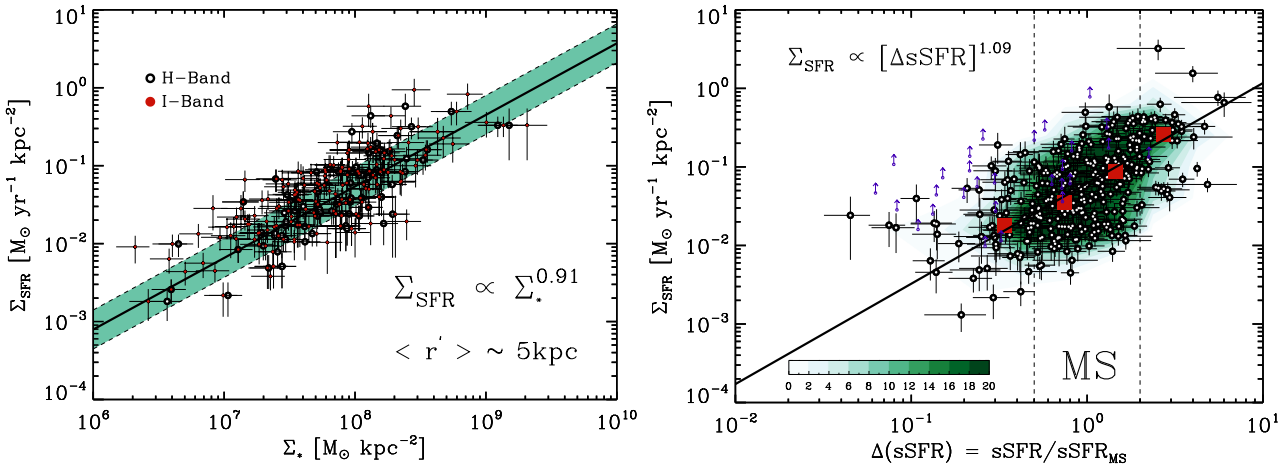

Figure 3. Left: a 'resolved' (down to, on average, ≈5.0 kpc) version of the star formation MS, showing the projected SFR density as a function of stellar density. It appears that the correlation between the ongoing and past star formation activity, as observed in the integrated properties of the galaxies holds at subgalactic scales. The black solid and dashed lines represent the best fit to the data and the corresponding scatter (0.25 dex). Right: projected SFR density as a function of distance from the MS. The black line corresponds to the best fit to the data, with a slope 1.09. The red boxes corresponds to the mean Σ_{SFR} in four Δ(sSFR) bins [$0.1 \leq \Delta(sSFR) < 0.5$, $0.5 \leq \Delta(sSFR) < 1$, $1 \leq \Delta(sSFR) \leq 2$ and $2 < \Delta(sSFR) < 10$]. The vertical dashed lines enclose the area of the MS, while the green contours depict the number density of the sources in the plot. Purple arrows correspond to lower limits for spatially unresolved sources with Hα detection. This plot demonstrates that, on average, galaxies with elevated sSFR with respect to the MS, are characterized by denser star formation activity.

per unit area, of our sources. We define the star formation surface density as

$$\Sigma_{SFR} = SFR/2\pi r_{1/2}^2 \quad [M_\odot\,yr^{-1}\,Mpc^{-2}]. \tag{4}$$

Similarly, for the subsample of our sources with available high-resolution *HST*-WFC3 H_{F160W}-band imaging, we infer their stellar mass density (Σ_*), using the morphological analysis of Van der Wel et al. (2012). In particular, using the Sercic index, the half-light radius (r_H) and the H_{F160W}-band magnitude of the sources, as derived by Van der Wel et al. (2012) we infer the amount of light, and subsequently the stellar mass within the Hα half-light radius of the galaxies, by assuming a constant mass-to-light ratio and rescaling the total stellar mass as derived from the galaxy-integrated SED-fitting. An obvious caveat is that while the H_{F160W}-band (rest frame 0.8 μm at $z \sim 1$) is in general sensitive to the stellar emission, the distribution of the stellar mass could be different from that of the H_{F160W}-band light, especially in high-resolution images. For example, Wuyts et al. (2013) find that at a 0.7 kpc resolution, the stellar mass of $z \sim 1.0$ star-forming galaxies is more centrally concentrated than the H_{F160W}-band light profile. However, at a scale of 5.0 kpc (which is the median $r'_{1/2}$ of the galaxies in our sample) we expect this effect to be less pronounced. In fact, we find that the Hα half-light radius is, on average, 1.3 times larger than that of the stellar light (r_H) (in agreement with Nelson et al. 2012). This means that we rescale the total stellar mass to that embedded within a radius $R > r_H$. Therefore, even if the stellar distribution is more centrally concentrated, we integrate over a significant portion of the galaxy, smoothing out, to a large degree at least, possible variations in the *M*/*L*.

In Fig. 3 (left) we plot Σ_{SFR} versus Σ_* showing a 'resolved' version, of the well-established galaxy-integrated SFR–M_* relation. Clearly, the correlation between the ongoing and past star formation activity appears to hold in subgalactic scales, down to ∼5.1 kpc (which is the average Hα half-light radius of our sample), with a slightly sublinear slope:

$$\log(\Sigma_{SFR}[M_\odot\,yr^{-1}\,kpc^{-2}]) = -8.21 + 0.91\log(\Sigma_*[M_\odot\,kpc^{-2}]. \tag{5}$$

To test against any possible bias introduced by the H_{F160W}-band observations. we also repeat the analysis using this time stellar size estimates based on ACS *F*840*W*-band imaging. As shown in Fig. 3 (left), the trend between Σ_{SFR} and Σ_* remains overall unaffected by the adopted band used to infer stellar size measurements.

The correlation between (Σ_{SFR}) and (Σ_*) that we derive here, is in excellent agreement with the slope of the galaxy-integrated MS (e.g. Whitaker et al. 2012), albeit without the flattening at the high-mass end, possibly due to the absence of galaxies with high stellar density in our sample. A flattening in the high stellar density end of the resolved MS is however reported in Wuyts et al. (2013), that used 3D-HST and CANDELS data for a sample of $z \sim 1$ star-forming galaxies. While the slope of the resolved MS reported by Wuyts et al. (2013) is very similar to that obtained here, we stress that the resolution of our data is ∼5 coarser than that of Wuyts et al. (2013) and any comparison between the two studies should be treated with caution. We conclude that the past and ongoing star formation follow closely each other not only in galactic but also in subgalactic scales, suggesting that over the same area, the rate of star formation tracks the amount of assembled stellar mass.

4.2 SFR surface density along the MS

The Σ_{SFR} in our sample spans approximately two orders of magnitude, suggesting a wide range of combinations between SFR and $r'_{1/2}$ for our galaxies. Several studies have attempted to investigate these variations of Σ_{SFR} as a function of sSFRs or, equally of distance to the MS. For example Wuyts et al. (2011), using stellar continuum sizes report a correlation between Σ_{SFR} and sSFR. Similarly, Elbaz et al. (2011), using radio size measurements, find a positive correlation between the two parameters, in the sense that galaxies with higher Σ_{SFR} tend to be have higher IR8 and sSFR. Here, we are in position to address this question using the Hα size measurements, that directly probe the area in which star formation is taking place, of ∼400 galaxies with resolved Hα emission.

In Fig. 3 (right) we plot the derived star formation surface densities as a function of the distance to the MS (Δ(sSFR)), by comparing

the sSFRs of the sources to a characteristic $sSFR_{MS}$ that varies with stellar mass and redshift of each source, following the Speagle et al. (2014) formula. This plot brings together the global star formation per unit stellar mass (sSFR) with the density of the star activity (Σ_{SFR}) and therefore can provide information about the geometry and the mode of star formation (stabursting). For unresolved sources with Hα measurement, we consider a lower limit of their Σ_{SFR} by adopting an upper $r'_{1/2}$, equal to the resolution element of the corresponding observation. We find a significant correlation (Spearman's test p-value $= 3 \times 10^{-19}$) between Σ_{SFR} and Δ(sSFR), with increasing (decreasing) star formation surface densities as we depart above (below) the MS. In particular a least-squares regression fit to the data yield $\Sigma_{SFR} \propto \Delta(\mathrm{sSFR})^{1.09}$ suggesting, on average, a variation in the star formation density of a factor of ~ 4 within the width of the MS (0.3 dex).

The increase of Σ_{SFR} for increasing SFR at a fixed stellar mass, suggests that galaxies form more stars per unit area as we move above the MS. This can be attributed to either an increase in the star formation efficiency (SFE $=$ SFR/M_{gas}), or an increase in the gas fraction of the galaxies f_{gas}, or a combination of the two. Various studies have shown that at fixed stellar mass, the gas fraction of MS galaxies increases for increasing SFR (e.g. Magdis et al. 2012; Genzel et al. 2015). For example Magdis et al. (2012) report a trend of increasing M_{gas}/M_* (or equally of f_{gas}) with increasing Δ(sSFR), with a slope of $\xi \approx 0.9$. On the other hand, Saintonge et al. (2011) and Genzel et al. (2015) find that as galaxies above the MS are characterized by shorter gas depletion time-scales, suggesting that the width of the MS is a combination of higher gas fractions and higher SFEs. While in the current study we cannot disentangle between the two processes, as we lack M_{gas} measurements, we confirm that measuring the sSFR of the galaxies with respect to the $sSFR_{MS}$ carries important information regarding the star formation activity in the galaxies and that the width of the MS is not just an artefact produced by random noise, but a manifestation of the variation of the physical properties of the MS galaxies.

Finally, we also find that starbursting galaxies are on average more compact than the MS galaxies, with a mean size of 4.2 ± 0.5 and 5.2 ± 0.3 kpc, respectively. This trend, i.e. starbursting being more compact than MS galaxies, is consistent with Elbaz et al. (2011) who used ACS V-band stacks (i.e. rest-frame UV for $z \sim 1$ galaxies). As discussed in Section 2, unresolved galaxies in our sample are predominantly passive galaxies (red $r - z$ colours, high stellar masses, low SFRs) which typically tend to have more concentrated light profiles. Therefore, it is not surprising to find a lot of unresolved galaxies lying below the MS. On the other hand, since starburst galaxies are on average smaller than MS galaxies, one could expect to see some unresolved systems above the MS too. However, Elbaz et al. (2011) report an average UV size for starbursting systems [Δ(sSFR) > 2] of 3.3 kpc, dropping down to 2.5 kpc when only strong starbursts are considered [Δ(sSFR) > 3]. In both cases, the average size of galaxies above the MS is well above the typical resolution achieved in KROSS. This, along with the fact that our sample lacks strong outliers above the MS [almost all galaxies have Δ(sSFR) < 4], could explain why all starbursts in our sample are resolved.

4.3 Metallicity gradient along the MS

Finally, using the gas phase abundance of oxygen [12+log(O/H)] in our galaxies, as derived in Section 3, we can investigate possible trends between the metallicity and the distance from the MS.

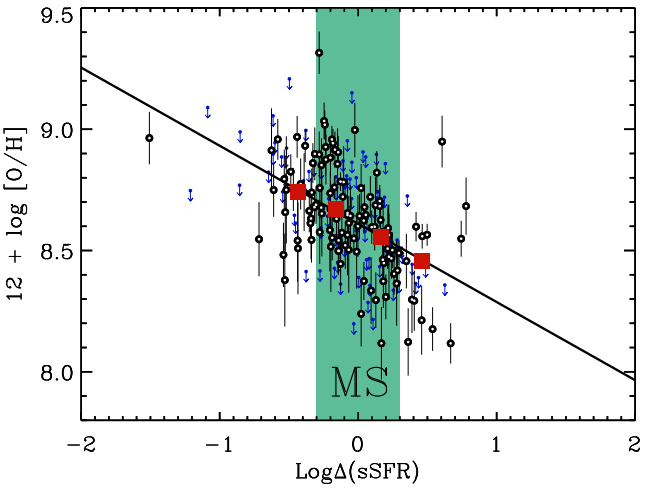

Figure 4. Metallicity versus distance from the MS. The red boxes correspond to the mean metallicity values in four Δ(sSFR) bins; one below, two within and one above the MS (same as in Fig. 3, right). The green shaded region depicts the locus of MS. The solid line represents the best fit to the data, with a slope of -0.36, suggesting a variation of 0.2 dex in the metallicity of the galaxies within the MS and significantly lower metallicities for star-bursting galaxies that sit well above the MS.

Indeed, Ellison et al. (2008), were the first to show an anticorrelation between metallicity and sSFR at fixed stellar mass. Follow-up studies, using SDSS data have further examined this trend, suggesting that the scatter around the well-established metallicity–stellar mass relation is correlated to the SFR of the galaxies (e.g. Yates, Kauffmann & Guo 2012; Andrews & Martini 2013; Salim et al. 2014). To this extent, Mannucci et al. (2010), established a fundamental, redshift-invariant, relation between SFR–M_*–Z, the so-called FMR relation, showing that at fixed stellar mass the metallicity of the galaxies decreases for increasing SFR. More recently, Salim et al. (2014), also presented evidence that metallicity is anti-correlated with sSFR regardless of the metallicity indicators used. Here, we can extend this investigation to high-z galaxies (see also Stott et al. 2013b).

In Fig. 4, we plot the metallicity as a function of distance from the MS, for galaxies in the stellar mass range of $9.5 < \log(M_*/\mathrm{M}_\odot) < 10.5$. The stellar mass bin was adopted in order to minimize the dependence on the stellar mass. Evidently, and in agreement with what is observed in the local Universe, at fixed stellar mass, galaxies with higher SFR (or equally for galaxies departing from the MS) are found to have lower metallicities. A linear regression fit to the data yields $Z \propto (\Delta(\mathrm{sSFR}))^{-0.32}$, suggesting a variation of $\sim$0.2 dex within the MS, and significantly lower metallicities for starbursting galaxies that sit well above the MS.

The observed trend can be explained via gas flows: galaxies with higher SFR at a fixed stellar mass are likely to experience higher accretion rates of pristine gas that dilute the metallicity content of the galaxies. For example in the model of Finlator & Davé (2008), it is proposed that for a given stellar mass, all galaxies have an equilibrium metallicity, and deviations from that are caused by inflow of pristine gas from the Inter Galactic Medium. In this scenario, we would expect higher gas surface densities and therefore higher Σ_{SFR}, something that is validated in the previous analysis. To this direction, Stott et al. (2014) find a correlation between the gaseous metallicity gradient and sSFR of a galaxy using the KMOS SV data and literature measurements. They find that central metallicity

is lower in high sSFR galaxies suggesting that this pristine gas is funnelled towards the core of these galaxies enhancing their SFRs. Furthemore, Bothwell et al. (2013) and De Rossi et al. (2015) presented evidence that the mass–metallicity relation exhibits a strong secondary dependence on total gas mass, rather than on SFR, with galaxies with higher gas fraction having lower metallicities. In this case, the deviation from the MS reflects variations in the gas fraction of the galaxies, as already discussed in the previous subsection. On the other hand, as argued by Ellison et al. (2008), the observed trend could also be driven by SFE variations; higher gas densities could have led to higher SFEs in the past ($z > 1$) that would yield higher metallicities for galaxies with lower SFR by $z = 1$. Again, as for the $\Sigma_{\rm SFR}$–Δ(sSFR) relation, while we recover a clear correlation between Z and Δ(sSFR), we need $M_{\rm gas}$ measurements in order to understand the physical mechanisms behind the observed trends.

Finally, Ellison et al. (2008) provides evidence that at given stellar mass larger galaxies have on average smaller metallicities, suggesting a secondary (but weaker to sSFR) dependence of the gas metallicity on the physical size of the galaxies. However, when we split our subsample of resolved galaxies with a gas metallicity measurement in various stellar mass bins, we do not recover a statistically significant correlation (or anticorrelation thereof) between the gas metallicity and $r'_{1/2}$. However, we note that the lack of anticorrelation between these two parameters is probably driven by (1) the small number of galaxies that populate in each stellar mass bin and (2) the fact that the range of the physical sizes of the galaxies in our sample is much narrower than that of the aforementioned studies (80 per cent of the galaxies with measured metallicities have 3 kpc $< r'_{1/2} <$ 7 kpc). Full treatment of the metallicity of the KROSS sample will be presented in Stott et al. (in preparation).

5 SUMMARY

We have presented first results from the ongoing KROSS survey, that targets ∼1000 star-forming galaxies at $z \sim 1$ with KMOS in order to detect and resolve their Hα emission. Using Hα flux densities and Hα size measurements as well as [N II] integrated flux densities for ∼500 observed galaxies so far, we have investigated various physical properties with respect to the MS of star formation. The main findings are as follows.

(i) Based on Hα flux density measurements we derive SFR estimates for galaxies in our sample and recover the SFR–M_* relation at $z \sim 1$ with a scatter of 0.3 dex, in agreement with previous studies.

(ii) Using Hα maps we measure the half-light radius of the galaxies and present a 'resolved' version of the MS of star formation that appears to hold with the same slope and scatter in subgalactic scales.

(iii) We find a strong correlation between the $\Sigma_{\rm SFR}$ and the distance from the MS, parametrized as Δ(sSFR) = sSFR/sSFR$_{\rm MS}$; galaxies tend to be characterized by denser star formation as we move above the MS.

(iv) We find a clear trend between the metallicity of the galaxies and their SFR at a fixed stellar mass (or equally their distance from the MS). The recovered relation suggests lower metallicities for galaxies well above the MS and a metallicity gradient of ∼0.2 dex within the MS.

Follow-up observations of the current sample to derive $M_{\rm gas}$ estimates, either through submm continuum observations or direct CO detections will enable us to understand the physical origin of the above trends.

ACKNOWLEDGEMENTS

We would like to thank the referee for carefully reading the manuscript and providing valuable comments and suggestions. GEM acknowledges support from STFC through grant ST/K00106X/1, the John Fell Oxford University Press (OUP) Research Fund and the University of Oxford. JPS, CMH and IRS acknowledge support from STFC (ST/I001573/1). JPS also acknowledges support from a Hintze Research Fellowship. IRS acknowledges support from an ERC Advanced Investigator programme DUSTYGAL and a Royal Society/Wolfson Merit Award. AJB gratefully acknowledges the hospitality of the Research School of Astronomy and Astrophysics at the Australian National University, Mount Stromlo, Canberra where some of this work was done under the Distinguished Visitor scheme. DS acknowledges financial support from the Netherlands Organization for Scientific research (NWO) through a Veni fellowship and from FCT through an FCT Investigator Starting Grant and Start-up Grant (IF/01154/2012/CP0189/CT0010). We thank Ian Smail for coordinating the efforts of the KROSS survey and for stimulating discussions. We thank Holly Elbert and Timothy Green for their observations and Matthieu Schaller for providing the EAGLE simulation quantities. GEM thanks Ryan Houghton and Borris Haussler for helpful discussions. Based on observations made with ESO Telescopes at the La Silla Paranal Observatory under the programme IDs 60.A-9460, 092.B-0538, 093.B-0106 and 094.B-0061.This research uses data from the VIMOS VLT Deep Survey, obtained from the VVDS data base operated by Cesam, Laboratoire dAstrophysique de Marseille, France. This paper uses data from the VIMOS Public Extragalactic Redshift Survey (VIPERS). VIPERS has been performed using the ESO Very Large Telescope, under the 'Large Programme' 182.A-0886. The participating institutions and funding agencies are listed at http://vipers.inaf.it. This paper uses data from zCOSMOS which is based on observations made with ESO Telescopes at the La Silla or Paranal Observatories under programme ID 175.A-0839. We thank D. Sobral and M. Cirasuolo for help with the survey.

REFERENCES

Andrews B. H., Martini P., 2013, ApJ, 765, 140
Bothwell M. S., Maiolino R., Kennicutt R., Cresci G., Mannucci F., Marconi A., Cicone C., 2013, MNRAS, 433, 1425
Brinchmann J., Charlot S., White S. D. M., Tremonti C., Kauffmann G., Heckman T., Brinkmann J., 2004, MNRAS, 351, 1151
Bruzual G., Charlot S., 2003, MNRAS, 344, 1000
Calzetti D., Armus L., Bohlin R. C., Kinney A. L., Koornneef J., Storchi-Bergmann T., 2000, ApJ, 533, 682
Cardamone C. N. et al., 2010, ApJS, 189, 270
Chabrier G., 2003, ApJ, 586, L133
Cirasuolo M. et al., 2007, MNRAS, 380, 585
Daddi E. et al., 2007, ApJ, 670, 156
Daddi E. et al., 2010, ApJ, 714, L118
Davies R. I. et al., 2013, A&A, 558, 56
De Looze I. et al., 2014, A&A, 568, A62
De Rossi M. E., Theuns T., Font A. S., McCarthy I. G., 2015, MNRAS, 452, 486
Díaz-Santos T. et al., 2010, ApJ, 723, 993
Díaz-Santos T. et al., 2013, ApJ, 774, 68
Elbaz D. et al., 2007, A&A, 468, 33
Elbaz D. et al., 2011, A&A, 533, 119
Ellison S. L., Patton D. R., Simard L., McConnachie A. W., 2008, ApJ, 672, L107
Finlator K., Davé R., 2008, MNRAS, 385, 2181

Garilli B. et al., 2008, A&A, 486, 683
Garilli B. et al., 2014, A&A, 562, A23
Genzel R. et al., 2010, MNRAS, 407, 2091
Genzel R. et al., 2015, ApJ, 800, 20
González V., Labbé I., Bouwens R. J., Illingworth G., Franx M., Kriek M., Brammer G. B., 2010, ApJ, 713, 115
Gracia-Carpio J. et al., 2011, ApJ, 728, L7
Guzzo L. et al., 2014, A&A, 566, A108
Häußler B. et al., 2007, ApJS, 172, 615
Hung C.-L. et al., 2013, ApJ, 778, 129
Kennicutt R. C., Jr, 1998, ARA&A, 36, 189
Kewley L. J., Dopita M. A., 2002, ApJS, 142, 35
Kewley L. J., Heisler C. A., Dopita M. A., Lumsden S., 2001, ApJS, 132, 37
Kim J.-W., Edge A. C., Wake D. A., Stott J. P., 2011b, MNRAS, 410, 241
Larson D. et al., 2011, ApJS, 192, 16
Lawrence A. et al., 2007, MNRAS, 379, 1599
Le Fèvre O. et al., 2005, A&A, 439, 845
Le Fèvre O. et al., 2013, A&A, 559, A14
Lehmer B. D. et al., 2005, ApJS, 161, 21
Lilly S. J. et al., 2007, ApJS, 172, 70
Magdis G. E., Rigopoulou D., Huang J.-S., Fazio G. G., 2010, MNRAS, 401, 1521
Magdis G. E. et al., 2012, ApJ, 760, 6
Magdis G. E. et al., 2014, ApJ, 796, 63
Magnelli B. et al., 2014, A&A, 561, A86
Mancini C. et al., 2011, ApJ, 743, 86
Mannucci F., Cresci G., Maiolino R., Marconi A., Gnerucci A., 2010, MNRAS, 408, 2115
Muzzin A. et al., 2013, ApJS, 206, 8
Nelson E. J. et al., 2012, ApJ, 747, L28
Noeske K. G. et al., 2007, ApJ, 660, L43
Nordon R. et al., 2012, ApJ, 745, 182
Pannella M. et al., 2009, ApJ, 698, L116
Peng C. Y., Ho L. C., Impey C. D., Rix H.-W., 2002, AJ, 124, 266
Pettini M., Pagel B. E. J., 2004, MNRAS, 348, L59
Rousselot P., Lidman C., Cuby J.-G., Moreels G., Monnet G., 2000, A&A, 354, 1134
Saintonge A. et al., 2011, MNRAS, 415, 61
Salim S., Lee J. C., Ly C., Brinchmann J., Davé R., Dickinson M., Salzer J. J., Charlot S., 2014, ApJ, 797, 126
Schreiber C. et al., 2015, A&A, 575, A74
Scoville N. et al., 2007, ApJS, 172, 1
Sharples R. et al., 2013, The Messenger, 151, 21
Simpson J. M. et al., 2014, ApJ, 788, 125
Smail I., Sharp R., Swinbank A. M., Akiyama M., Ueda Y., Foucaud S., Almaini O., Croom S., 2008, MNRAS, 389, 407
Sobral D., Best P. N., Matsuda Y., Smail I., Geach J. E., Cirasuolo M., 2012, MNRAS, 420, 1926
Sobral D., Smail I., Best P. N., Geach J. E., Matsuda Y., Stott J. P., Cirasuolo M., Kurk J., 2013, MNRAS, 428, 1128
Sobral D. et al., 2015, MNRAS, 451, 2303
Speagle J. S., Steinhardt C. L., Capak P. L., Silverman J. D., 2014, ApJS, 214, 15
Steidel C. C., Adelberger K. L., Dickinson M., Giavalisco M., Pettini M., Kellogg M., 1998, ApJ, 492, 428
Stott J. P., Sobral D., Smail I., Bower R., Best P. N., Geach J. E., 2013a, MNRAS, 430, 1158
Stott J. P. et al., 2013b, MNRAS, 436, 1130
Stott J. P. et al., 2014, MNRAS, 443, 2695
Swinbank A. M., Smail I., Sobral D., Theuns T., Best P. N., Geach J. E., 2012, ApJ, 760, 130
Tasca L. A. M. et al., 2009, A&A, 503, 379
Tiley et al., 2015, MNRAS, submitted
van der Wel A. et al., 2012, ApJS, 203, 24
Whitaker K. E., Kriek M., van Dokkum P. G., Bezanson R., Brammer G., Franx M., Labbé I., 2012, ApJ, 745, 179
Whitaker K. E. et al., 2014, ApJ, 795, 104
Wuyts S. et al., 2011, ApJ, 738, 106
Wuyts S. et al., 2013, ApJ, 779, 135
Yates R. M., Kauffmann G., Guo Q., 2012, MNRAS, 422, 215

This paper has been typeset from a TEX/LATEX file prepared by the author.